Article

Synthesis, Luminescence and Energy Transfer Properties of Ce³⁺/Mn²⁺ Co-Doped Calcium Carbodiimide Phosphors

Erwan Leysour de Rohello [1], **Yan Suffren** [1], **Francis Gouttefangeas** [2], **Odile Merdrignac-Conanec** [1], **Olivier Guillou** [1] and **François Cheviré** [1,*]

[1] Univ Rennes 1, INSA Rennes, CNRS, ISCR (Institut des Sciences Chimiques de Rennes)—UMR 6226, F 35000 Rennes, France
[2] Univ Rennes 1, CNRS, ScanMAT—UAR 2025, F 35000 Rennes, France
* Correspondence: francois.chevire@univ-rennes.fr

Abstract: Ce³⁺-doped and Ce³⁺/Mn²⁺ co-doped calcium carbodiimide ($CaCN_2$) phosphors were synthesized from doped calcium carbonate and carbon nitride by a solid-state reaction at 700 °C under flowing NH_3 using a very short reaction time (1 h). The samples were characterized by powder X-ray diffraction, scanning electron microscopy and their diffuse reflectance and luminescence properties were investigated. Single-doped $CaCN_2$:Ce³⁺ exhibits a blue emission under near-ultraviolet activation (386 nm) corresponding to the $5d^1 \rightarrow {}^2F_{5/2}$ and $5d^1 \rightarrow {}^2F_{7/2}$ transitions of Ce³⁺. Maximum emission is obtained at temperatures lower than 150 K and then progressively decreases up to 387 K, with an 80% drop in the emission at room temperature. Efficient energy transfers from Ce³⁺ to Mn²⁺ via a non-radiative dipole–dipole mechanism are evidenced for the co-doped samples, leading to various colored phosphors under near-ultraviolet activation (386 nm). The emission color of the obtained phosphors can be modulated from blue to red through a shade of white depending on the sensitizer/activator ratio.

Keywords: carbodiimides; phosphors; co-doping; carbon nitride; energy transfer; cerium

1. Introduction

Light-emitting diodes (LEDs) are considered as indispensable solid-state light sources for the next generation of lighting. In this current era of energy saving and sustainable development, LEDs represent a green alternative to other conventional lighting systems used nowadays. In particular, LEDs have some advantages over fluorescent and incandescent lamps such as high efficiency, energy saving, long operation lifetime and mercury free. Nowadays, conventional white LEDs are made up of a blue LED chip (GaN/InGaN) coated with a yellowish light-emitting phosphor ($Y_3Al_5O_{12}$:Ce³⁺, YAG:Ce³⁺). However, the light produced by such devices lacks some red emission component, which results in a bad rendering of the colors of the illuminated objects and high correlated color temperature [1,2]. In addition, recent studies have reported that prolonged exposure to artificial blue-rich white light can have a harmful effect on mental alertness, circadian rhythm, metabolism and mood patterns as the photosensitive ganglion cells in the retina signal the brain to stop producing melatonin [3,4]. To overcome these problems, the development of blue, red and green phosphors that can be excited by near-ultraviolet (near-UV) light-emitting diodes has been largely investigated within the past decade. Nonetheless, to date, the strategy of using multiphosphors usually suffers from several drawbacks which are a high manufacturing cost, the trade-off in luminous efficiency attributed to re-absorption among the different phosphors and the non-uniformity of luminescent properties within the phosphor mixture, leading to color alteration [5,6]. Hence, many efforts have been devoted to design single-phase white light-emitting phosphors, which have benefits, such as good emission color stability and high color rendering index [7–10].

Over the last decade, inorganic carbodiimide materials with the general formula $M_x(NCN)_y$ (M = alkali, alkaline-earth, rare-earth or transition metals) have emerged as potential materials for lighting due to their remarkably high thermal and chemical properties [11–20]. More particularly, the emission properties of rare earth elements involving *5d-4f* electronic transitions, i.e., Eu^{2+} and Ce^{3+}, were recently investigated in various carbodiimides hosts such as $SrCN_2$:Eu^{2+} (orange red) [14–16], $BaCN_2$:Eu^{2+} (red) [17] or $Gd_2(CN_2)_3$:Ce^{3+} (yellow) [11] with activation capabilities in the near-UV-blue range. Since the involved *5d* orbitals are external, the position of these energy levels and, consequently, the wavelengths of excitation and emission bands strongly depend on the host lattices. As a nitrogen-containing pseudo-chalcogenide anion, the $[N=C=N]^{2-}$ group has an electronegativity value of 3.36 within those of N^{3-} and O^{2-}, 3.04 and 3.44, respectively [21,22], thus a lower nephelauxetic effect on activators *nd* states is expected compared to nitrides in regard to oxides hosts. A common carbodiimide compound is $CaCN_2$ used as fertilizer since the early 20th century and obtained from the reaction of CaC_2 with nitrogen at 1000 °C [23]. $CaCN_2$ crystallizes in the rhombohedral *R*3m space group (No. 166) and its crystal structure is displayed in Figure S1. In $CaCN_2$, the Ca^{2+} cation is octahedrally coordinated by nitrogen atoms within layers, that spray parallel to the (001) plane, formed by edge-sharing octahedra and connected by $[N=C=N]^{2-}$ carbodiimide units oriented along the *c*-axis. Additionally, recent studies have shown that $CaCN_2$:Mn^{2+} exhibits an intense red emission with acceptable thermal stability but only under high energy activation (λ < 300 nm), thus limiting its use as phosphor material for light-emitting devices [18,20]. In order to improve its activation behavior using the energy transfer approach and allow excitation at lower energy, this study focuses on the effect of Ce/Mn co-doping on its excitation and emission properties. To achieve this, $CaCN_2$:Ce^{3+} is first synthesized using the previously reported carbon nitride route [16] and its luminescence properties are discussed. Then, the impact of various Ce/Mn doping rates on the excitation and emission properties is investigated.

2. Results and Discussion

2.1. Materials Characterization and Optical Properties of $Ca_{1-x}Ce_xCN_2$ (0 ≤ x ≤ 0.04)

2.1.1. Materials Characterization

All $Ca_{1-x}Ce_xCN_2$ (x = 0, 0.003, 0.005, 0.01, 0.015, 0.02, 0.03 and 0.04) samples were identified by the X-ray powder diffraction technique (XRD). As shown in Figure 1, all compounds can be unambiguously indexed as rhombohedral phase (space group R3m, COD card no. 153-9974). Nonetheless, additional low-intensity lines indicate the presence of cerium oxycarbodiimide $Ce_2O_2CN_2$ (space group P3m1, JCPDS no. 049-1164) as a secondary phase for the sample with Ce^{3+} content greater than 2 mol%, as evidenced by the presence of lines (001), (101) and (102) located at 10.57°, 28.00° and 33.61°, respectively (zoom Figure 1). Rietveld refinement analyses were conducted on the as-prepared samples to verify the impact of cerium doping on the crystal lattice. The Rietveld refinement result for $CaCN_2$:0.5%Ce as well as details of the structural parameters and the atomic parameters are given in Figure S2 and Tables S1 and S2. The evolution of the *a* and *c* unit cell parameters as well as the cell volume versus the Ce^{3+} doping concentration are presented in Figure 2. Despite similar ionic radii between the Ca^{2+} and Ce^{3+} ions in 6-fold coordination, i.e., $r_{Ca^{2+}}$ = 1.00 Å and $r_{Ce^{3+}}$ = 1.01 Å [24], a slight increase in the cell parameters can be observed up to 2 mol% (Ce). The lattice parameters then remain more or less constant up to 4 mol% (Ce) due to the formation of $Ce_2O_2CN_2$ as a secondary phase indicating that the solubility limit of Ce^{3+} within the $CaCN_2$ matrix is quite limited. One reason can be the formal charge difference between the substituted cation Ca^{2+} and the dopant cation Ce^{3+}, resulting in local distortions and/or the creation of defects to maintain the overall electroneutrality of the crystal lattice, such as cationic vacancies according to the equation: $3\,Ca^{2+} \rightarrow 2\,Ce^{3+} + V_{Ca}$.
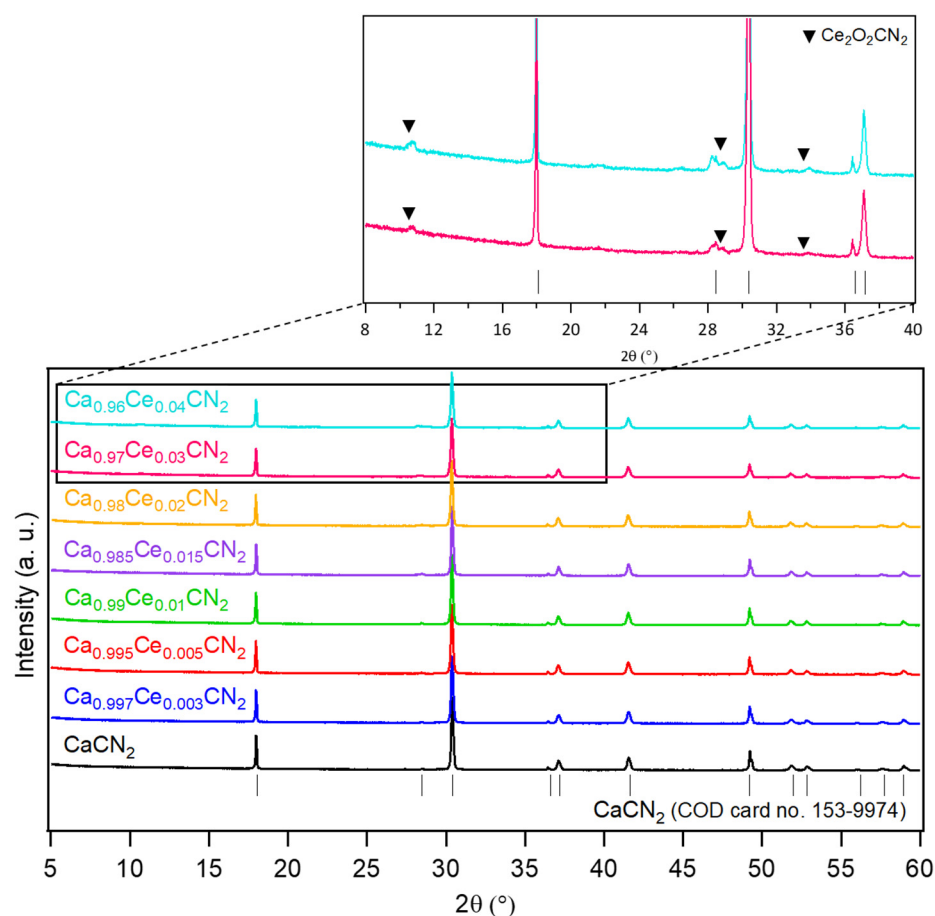
**Figure 1.** Powder X-ray diffraction diagrams of $Ca_{1-x}Ce_xCN_2$ ($0 \leq x \leq 0.04$) samples. Inset: Zoom on the X-ray diffraction diagrams of samples $Ca_{0.97}Ce_{0.03}CN_2$ and $Ca_{0.96}Ce_{0.04}CN_2$ between $8°$ and $40°$ (Inverted triangles (▼) indicate the main peaks of the $Ce_2O_2CN_2$ impurity (JCPDS no. 049 1164)).
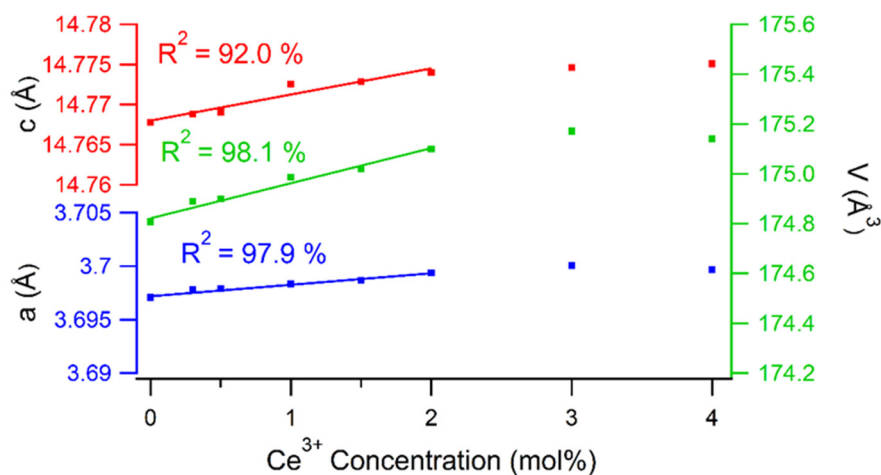
Figure 2. Evolution of the unit cell parameters (a, c) and cell volume (V) in $Ca_{1-x}Ce_xCN_2$ ($0 < x < 0.04$) samples versus Ce^{3+} doping concentration.

Scanning electron microscopy (SEM) images of the $Ca_{0.995}Ce_{0.005}CN_2$ sample, displayed in Figure 3, show comparable powder morphology to that observed in our previous work for $CaCN_2$ and $CaCN_2:Mn^{2+}$, i.e., agglomerates measuring up to 40 μm formed by well-rounded shaped crystallized elementary particles (Figure 3a,b) [20]. The latter, with size in the micron range, are strongly sintered despite the 1 h annealing dwell used during

the synthesis (Figure 3c). Additionally, the particles exhibit a layered texture on their surface in accordance with the 2D crystal structure of $CaCN_2$ (Figure 3d) [25].
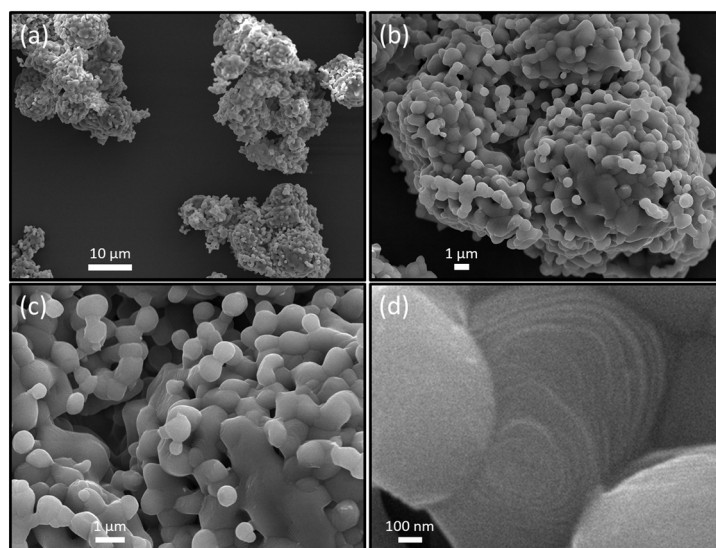
Figure 3. SEM images of $Ca_{0.995}Ce_{0.005}CN_2$ powder at various magnifications: (**a**) ×1500, (**b**) ×2500, (**c**) ×10,000 and (**d**) ×50,000.

Moreover, in order to confirm the amount of dopant as well as the nitrogen and oxygen contents, elemental analyses were performed on each sample using Energy dispersive X-ray spectroscopy (EDS) and the inert gas fusion technique, respectively (see Table 1). The EDS results reveal the presence of residual sodium from the carbonate precursors synthesized by co-precipitation from a sodium carbonate solution. Thus, Ce contents have been recalculated versus calcium content only (values in brackets) to compare with the targeted Ca/Ce ratios. Indeed, slightly higher Ce amounts are systematically observed in the samples. Note that as reported in our previous work [20], sodium can be removed by increasing the reaction temperature up to 800 °C but at the cost of the formation of stable CaO and MnO side-products. Moreover, removal of sodium does not improve the luminescence properties of the $CaCN_2$ based phosphors. On the other hand, nitrogen contents are consistent with calculated values within experimental errors. However, there is a downward trend in the latter in samples with values of $x \geq 0.03$, as well as an increase in the amounts of oxygen, both associated with the presence of the $Ce_2O_2CN_2$ impurity.

Table 1. Chemical composition and Ce^{3+} content of $Ca_{1-x}Ce_xCN_2$ ($0 < x < 0.04$) samples.

|	Ca at%	Ce at% *	Na at%	N_{exp} wt%	N_{calc} wt%	ΔN % **	O wt%
$Ca_{0.997}Ce_{0.003}CN_2$	98.83	0.45 (0.45)	0.72	34.45	34.83	1.09	0.51
$Ca_{0.995}Ce_{0.005}CN_2$	98.11	0.59 (0.60)	1.30	34.19	34.75	1.64	0.41
$Ca_{0.99}Ce_{0.01}CN_2$	96.47	1.28 (1.31)	2.25	35.34	34.53	2.34	0.78
$Ca_{0.985}Ce_{0.015}CN_2$	95.75	1.61 (1.65)	2.64	34.35	34.32	0.09	0.55
$Ca_{0.98}Ce_{0.02}CN_2$	95.19	2.17 (2.23)	2.64	33.23	34.11	2.58	0.41
$Ca_{0.97}Ce_{0.03}CN_2$	94.86	3.35 (3.41)	1.79	32.22	33.70	4.39	1.36
$Ca_{0.96}Ce_{0.04}CN_2$	91.86	4.76 (4.93)	3.38	31.77	33.30	4.59	1.22

* Values without brackets represent Ce^{3+} rates taking into account Na; the values in brackets are the Ce^{3+} rates recalculated without considering Na. ** Deviation of the experimental nitrogen rate from the theoretical value.

2.1.2. Optical Properties

The diffuse reflection spectra of the $Ca_{1-x}Ce_xCN_2$ samples ($0 \leq x \leq 0.04$) are shown in Figure 4. The doped samples show an absorption edge located at 250 nm corresponding to

the electronic transitions between the valence and conduction bands of the $CaCN_2$ host lattice [20]. Two absorption bands whose intensities increase with the cerium doping rate are observed between 265–340 nm and 370–450 nm, respectively. As these bands are not visible in the undoped sample, they can only be attributed to the $4f \rightarrow 5d$ transitions of the Ce^{3+} ion, thus indicating the effective reduction of cerium under the experimental conditions. Let us also note that samples with values of $x \geq 0.03$ show an additional absorption band between 450–600 nm, which is attributed to the absorption of the $Ce_2O_2CN_2$ impurity that is described as having a pale-yellow coloration according to its JCPDS data sheet (JCPDS no. 049-1164).
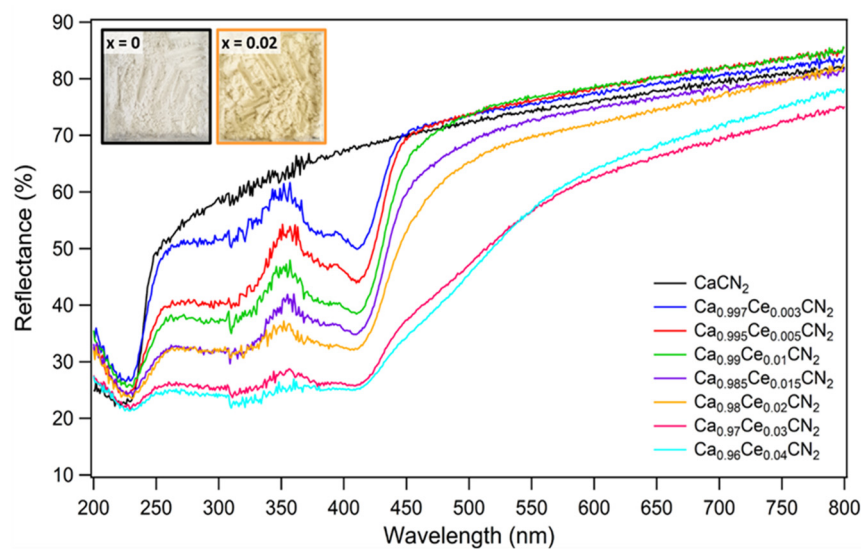

Figure 4. Diffuse reflection spectra of undoped and Ce^{3+}-doped $CaCN_2$ samples at room temperature. In inset: Appearance of $CaCN_2$ and $Ca_{0.98}Ce_{0.02}CN_2$ powders in daylight.

The normalized photoluminescence excitation (PLE) and emission (PL) spectra of the $Ca_{0.995}Ce_{0.005}CN_2$ sample at room temperature, as well as Commission Internationale de l'Éclairage (CIE) coordinates and a picture of the emitting phosphor under 365 nm UV lamp illumination are presented in Figure 5. When monitored with emission wavelength at 462 nm, the PLE spectrum shows a partially overlapping double band with maxima at 384 and 414 nm, respectively. These bands, which extend over a wavelength range from 350 to 450 nm are characteristic of the $4f \rightarrow 5d$ transitions of Ce^{3+} ion [26,27], in good agreement with the absorption bands observed on the diffuse reflection spectra. Under excitation at 386 nm, the emission spectrum of the sample consists of a broad asymmetric emission band from 400 to 650 nm whose maxima were estimated at 462 nm (main peak) and 510 nm by using a Gaussian fit which allows the deconvolution of the double band into two contributions (Figure S3). This gap of 48 nm (i.e., approximately 2040 cm^{-1} on an energy scale) between these two maxima is of the same order of magnitude as the theoretical value of 2000 cm^{-1} expected between the two $4f$ sublevels of trivalent cerium, and thus the double band can be ascribed to the $5d^1 \rightarrow {}^2F_{5/2}$ and $5d^1 \rightarrow {}^2F_{7/2}$ transitions [28]. The presence of a unique double band related to the cerium emission also indicates that the Ce^{3+} ion occupies only one site within the lattice, namely, the octahedrally coordinated Ca^{2+} site of the investigated host lattice. Such cyan emission is in good agreement with those already observed in sulfide and oxide matrices such as $SrS:Ce^{3+}$, $CaS:Ce^{3+}$ and $CaO:Ce^{3+}$ where the Ce^{3+} ion is located at the octahedral site [29,30]. The CIE chromaticity coordinates are ($x = 0.19$, $y = 0.29$).
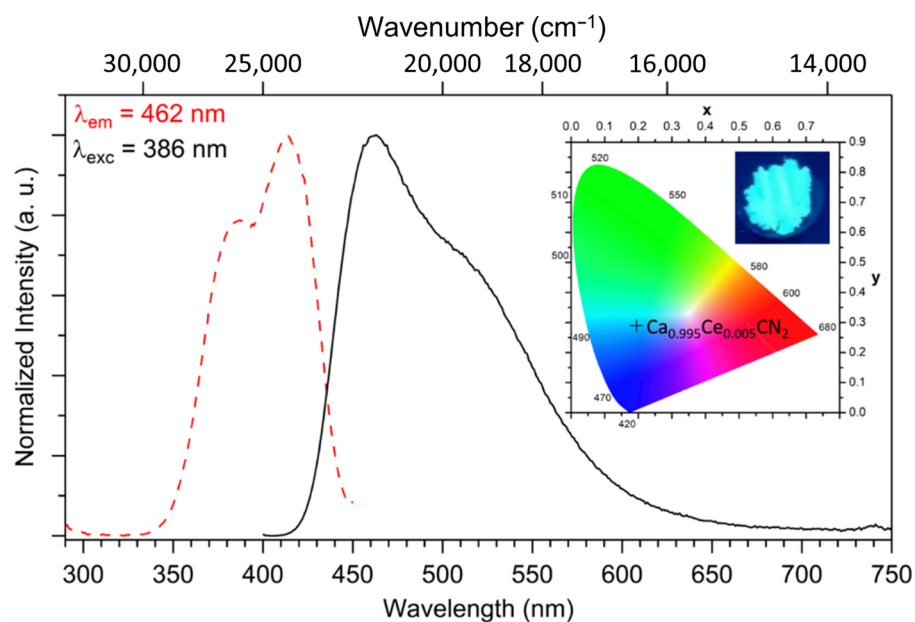
Figure 5. PLE and PL spectra at room temperature of the $Ca_{0.995}Ce_{0.005}CN_2$ sample. In inset: The CIE chromaticity diagram, chromaticity coordinates ($x = 0.19$, $y = 0.29$) and picture under 365 nm UV lamp.

A study of the photoluminescence properties at room temperature as a function of the Ce^{3+} dopant concentration was carried out in order to determine the optimum cerium concentration. Figure 6 shows the emission spectra of $Ca_{1-x}Ce_xCN_2$ ($x = 0.003$, 0.005, 0.01, 0.015, 0.02, 0.03 and 0.04) samples. While the profile of the emission peak does not vary with the Ce^{3+} content, the emission intensity of $Ca_{1-x}Ce_xCN_2$ phosphors strongly depends on it. The optimized Ce^{3+} doping concentration in the $CaCN_2$ host lattice is approximately 0.5 mol%. For higher content the emission intensity decreases continuously from 0.5 to 4 mol%. Several hypotheses could explain the observed decrease in emission intensity such as a concentration quenching effect, the formation of local distortions related to the charge difference between Ca^{2+} and Ce^{3+} increasing the probability of non-radiative relaxation or the presence of $Ce_2O_2CN_2$ as a secondary phase for doping rate greater than 2 mol%.
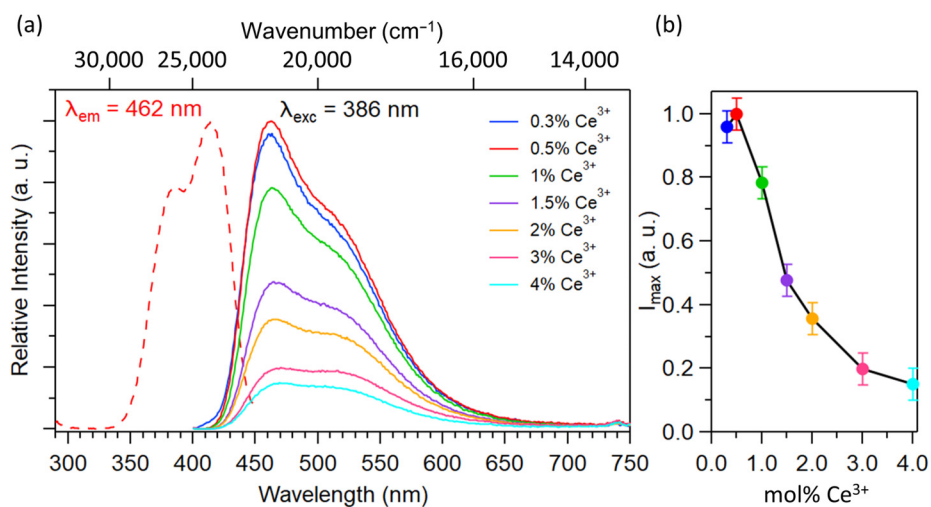
Figure 6. (**a**) PL spectra at room temperature of $CaCN_2$:Ce samples. (**b**) Maximum emission intensity (I_{max}) vs. mol% (Ce) for $CaCN_2$:Ce. Uncertainty bars = ±0.05.

In addition, the fluorescence decay time of Ce^{3+} in the $Ca_{0.995}Ce_{0.005}CN_2$ sample as well as the quantum yield have been measured at room temperature under excitation at

394 and 386 nm, respectively. As shown in Figure 7, the decay curves can be well fitted by a bi-exponential function. The associated decay times τ_1 and τ_2 are 3.0(1) ns and 7.3(1) ns with very close amplitudes, in agreement with the two possible transitions from the excited state to the $^2F_{5/2}$ and $^2F_{7/2}$ levels. Moreover, the nanosecond magnitude is comparable to what is usually measured in Ce^{3+}-doped phosphors [26,31,32]. The internal quantum yield (excitation via Ce^{3+}) has been estimated at 11.5(1.4)% under 386 nm excitation wavelength which is quite low for application as a phosphor in LED lighting that generally requires the highest possible efficiency.
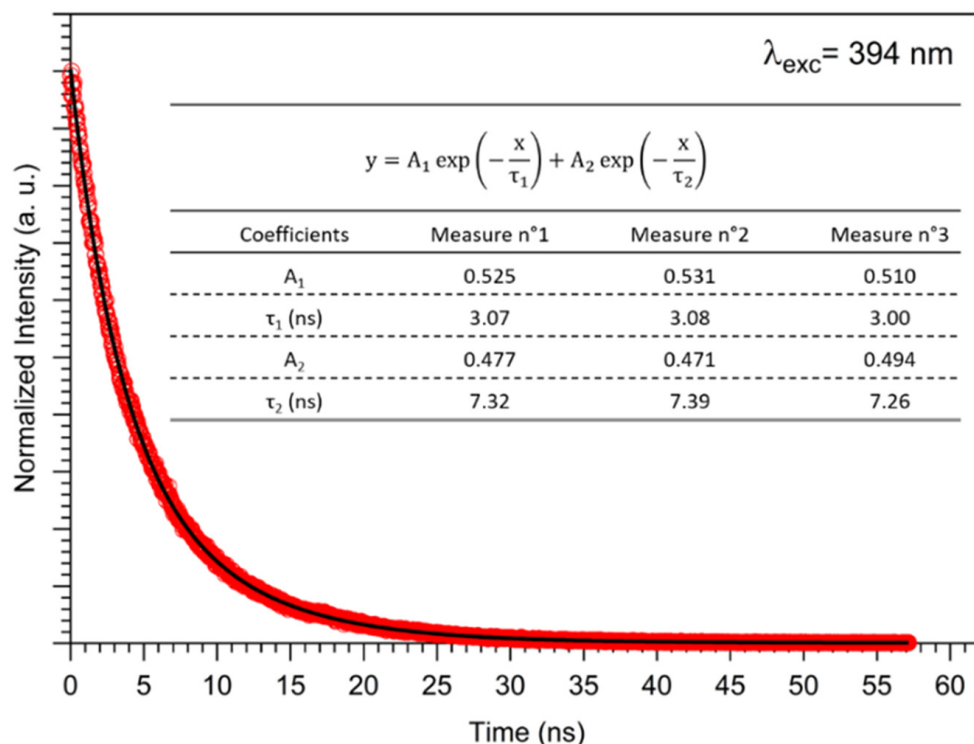

Figure 7. Luminescent decay measurement of $Ca_{0.995}Ce_{0.005}CN_2$ at 300 K under photoexcitation at 394 nm (red circles), bi-exponential curve fit (black line) and calculated decay times τ_1 and τ_2.

The effect of the temperature on the emission was investigated between 293 and 387 K under 386 nm excitation wavelength. As depicted in Figure 8, the emission intensity of $Ca_{0.995}Ce_{0.005}CN_2$ is decreasing rapidly by approximatively 80% up to 387 K. The temperature at which the emission intensity is reduced by 50% ($T_{1/2}$) is approximately 330 K. This phenomenon is completely reversible indicating that the loss of luminescence is not related to any degradation of the product under the measurement conditions as $CaCN_2$ is stable up to approximately 600 °C [20]. In light of the rapid decrease in emission intensity with increasing temperature and the low quantum yield at room temperature, a low-temperature study between 77 and 300 K was carried out in order to assess more accurately the thermal stability of the emission. The resulting emission spectra recorded at 386 nm are shown in Figure 9. It can be seen that the emission intensity is relatively stable up to 150 K before dropping to approximately 80% up to 300 K. Thus, these results show that a strong quenching of the luminescence is already occurring at room temperature, which can be correlated to the low quantum yield observed above. The reduction in emission intensity is attributed to higher probability of non-radiative transitions at higher temperature.
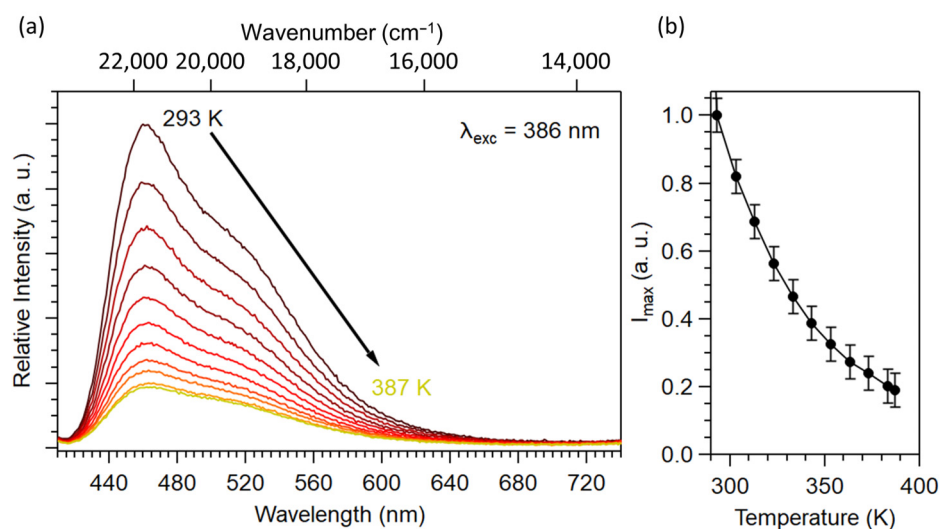
Figure 8. (**a**) PL spectra (λ_{exc} = 386 nm) of $Ca_{0.995}Ce_{0.005}CN_2$ at variable temperature (293–387 K). (**b**) Maximum emission intensity (I_{max}) vs. temperature (293–387 K) for $Ca_{0.995}Ce_{0.005}CN_2$. Uncertainty bars = ±0.05.
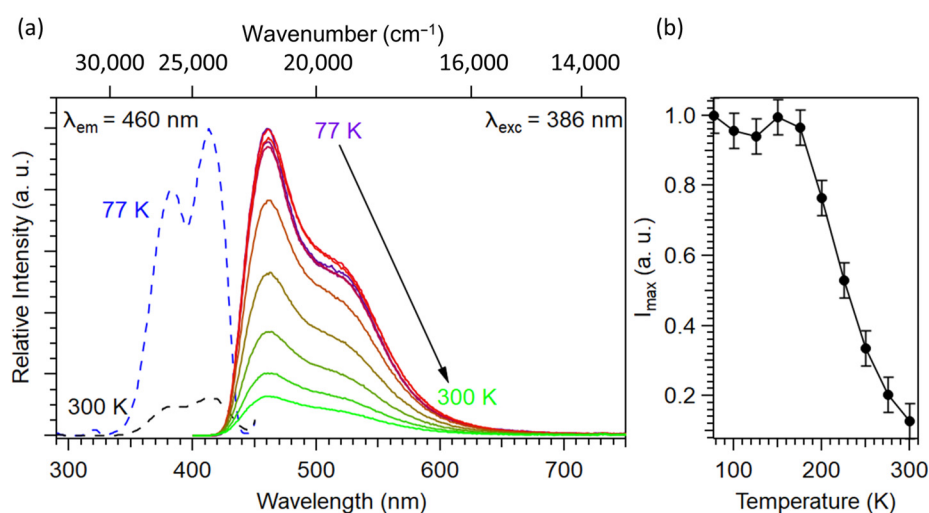

Figure 9. (**a**) PL spectra (λ_{exc} = 386 nm) of $Ca_{0.995}Ce_{0.005}CN_2$ at low temperature (77–300 K). (**b**) Maximum emission intensity (I_{max}) vs. temperature (77–300 K) for $Ca_{0.995}Ce_{0.005}CN_2$. Uncertainty bars = ±0.05.

2.2. Optical Properties of $Ca_{0.997-y}Ce_{0.003}Mn_yCN_2$ ($0.003 \leq y \leq 0.04$)

The structural characterizations and elemental analyses for the $Ca_{0.997-y}Ce_{0.003}Mn_yCN_2$ ($0.003 \leq y \leq 0.04$) samples are gathered in Figures S4–S6 and Tables S3 and S4. The obtained results are similar to those obtained for the Ce^{3+} and Mn^{2+} single-doped $CaCN_2$ samples and confirm the formation of single-phase compounds with the targeted Ce^{3+} and Mn^{2+} doping rates. Figure 10 shows the diffuse reflection spectra of $Ca_{0.997-y}Ce_{0.003}Mn_yCN_2$ ($0.003 \leq y \leq 0.04$) samples. One can find on the spectra of the co-doped samples the contributions of cerium and manganese previously observed on the series of samples single-doped with Mn^{2+} or Ce^{3+} [20]. First, the absorption edge located at 250 nm corresponds essentially to the electronic transitions between the valence and conduction bands of the $CaCN_2$ host lattice. Additionally, an absorption band around 260–280 nm which shifts to longer wavelengths with increasing manganese content can be attributed to the presence of $3d(Mn)$ levels in the band gap of the $CaCN_2$ matrix [20]. Finally, the two absorption bands between 265–340 nm and 370–450 nm are associated with the $4f \rightarrow 5d$ transitions of the Ce^{3+} ion as discussed above. The daylight color of co-doped samples

shows creamy-white to light-brown color depending on the Mn^{2+} doping rate as a result of the absorption in the visible range from electronic transitions between $3d$(Mn) states.
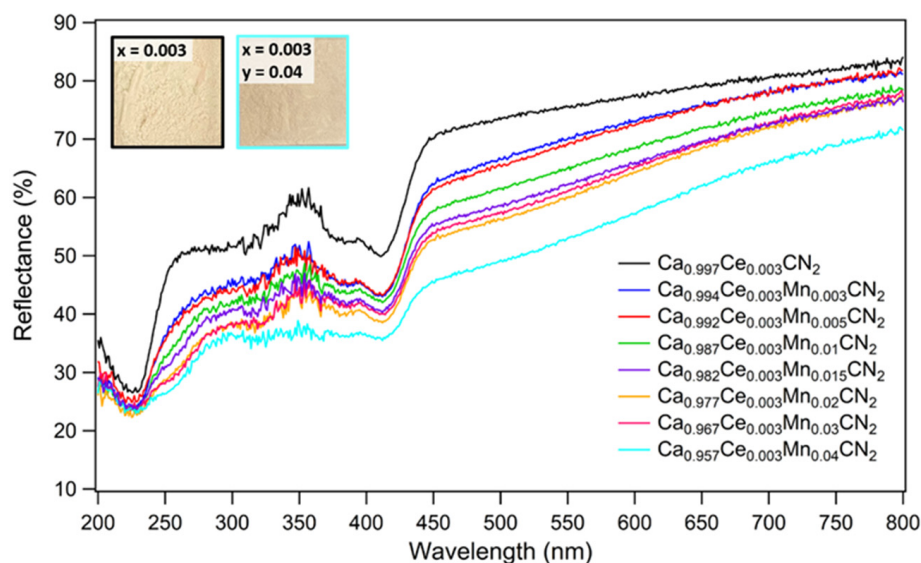
Figure 10. Diffuse reflection spectra of $Ca_{0.997}Ce_{0.003}CN_2$ and $Ca_{0.997-y}Ce_{0.003}Mn_yCN_2$ (0.003 $\leq y \leq$ 0.04) samples at room temperature. In inset: Appearance of $Ca_{0.997}Ce_{0.003}CN_2$ and $Ca_{0.957}Ce_{0.003}Mn_{0.04}CN_2$ powders in daylight.

The photoluminescence properties of the Ce^{3+}/Mn^{2+} co-doped samples were then studied. The obtained photoluminescence spectra are shown in Figure 11a. The excitation spectra of the $Ca_{0.987}Ce_{0.003}Mn_{0.01}CN_2$ sample were recorded by fixing the emission wavelength at 462 nm and 680 nm, respectively, while the normalized emission spectra of the whole series were recorded at 386 nm. The evolution of luminescence intensity as a function of manganese concentration is presented in Figure 11b. By monitoring the emission at 680 nm, the PLE spectrum of $Ca_{0.987}Ce_{0.003}Mn_{0.01}CN_2$ shows two excitation bands. The first one, located around 270 nm, is attributed to the absorption of the host lattice as already discussed in our previous study on Mn^{2+}-doped $CaCN_2$ [20]. The second, consisting of a partially overlapping double band between 350 and 450 nm, corresponds to the $4f \rightarrow 5d$ transitions of the cerium ion by analogy to the results obtained on the series of Ce^{3+}-doped $CaCN_2$ samples (see Figure 5). The presence of this absorption band on the excitation spectrum for the emission centered at 680 nm supports the occurrence of energy transfers from Ce^{3+} ions to Mn^{2+} ions, as single-doped $CaCN_2$:Mn^{2+} exhibits such emission at 680 nm only when excited through the host lattice at high energy, i.e., $\lambda \leq$ 270 nm [20]. Under excitation at 386 nm, the emission spectrum of $Ca_{0.987}Ce_{0.003}Mn_{0.01}CN_2$ (green line) shows the characteristic emission bands of both Ce^{3+} and Mn^{2+} ions. The first emission band located between 400 and 580 nm is the double band associated with the $5d^1 \rightarrow {}^2F_{5/2}$ and $5d^1 \rightarrow {}^2F_{7/2}$ transitions of Ce^{3+} while the second one centered at approximately 680 nm corresponds to the $^4T_{1g}(4G) \rightarrow {}^6A_{1g}(6S)$ transitions of Mn^{2+} [20].

Under excitation at 386 nm, the evolution of the profile of the PL spectra as a function of the Mn^{2+} ion concentration shows a progressive decrease in the Ce^{3+} emission intensity to the benefit of the Mn^{2+} one, which increases continuously from 0.3 to 2 mol% (Mn). From 3 mol% (Mn), the emission intensity decreases due to the self-extinction of the luminescence by concentration quenching as previously observed for single-doped $CaCN_2$:Mn^{2+} but at a lower Mn doping rate [20]. A similar behavior of the respective emission intensities associated with Ce^{3+} and Mn^{2+} ions has already been observed in other Ce^{3+}/Mn^{2+} co-doped lattices such as CaO:Ce^{3+},Mn^{2+} or $Sr_3La(PO_4)_3$:Ce^{3+},Mn^{2+} [29,33].

To quantify the optical characteristics of phosphors and to evaluate the impact of Mn^{2+} co-doping on the generated color, the chromaticity coordinates (x, y) of prepared materials have been determined. Numerical results are listed in Table S5, whereas the CIE

chromaticity diagram as well as a picture of the emitting phosphors under 365 nm UV lamp exposure are presented in Figure 12. The chromaticity coordinates of the series of samples show that a color gradient is obtained, varying from cyan (y = 0, 0.003 and 0.005) to red (y = 0.03 and 0.04) through a shade of white (y = 0.01), as a function of the increase in manganese rate.
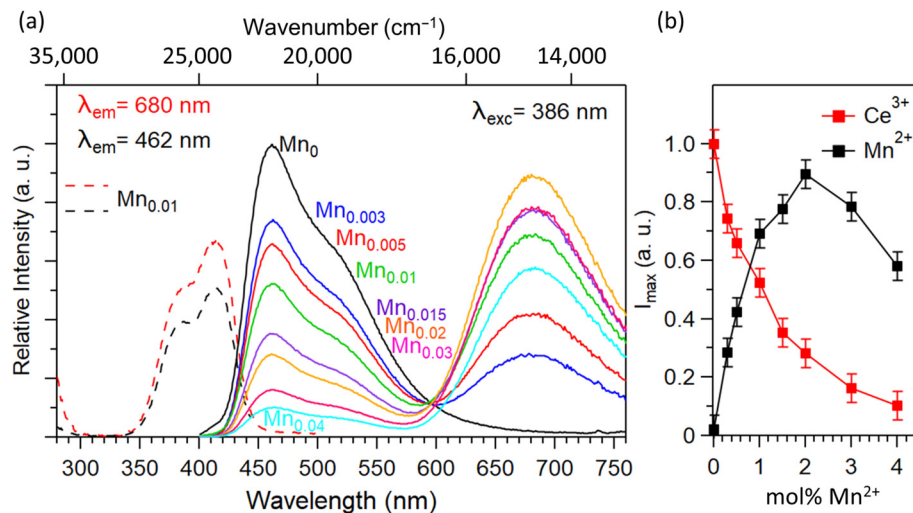
Figure 11. (**a**) PLE spectra monitored at 680 nm (red-dashed curve) and 462 nm (black-dashed curve) of $Ca_{0.987}Ce_{0.003}Mn_{0.01}CN_2$ and PL spectra (λ_{exc} = 386 nm) of $Ca_{0.997-y}Ce_{0.003}Mn_yCN_2$ ($0.003 \leq y \leq 0.04$) samples at room temperature. (**b**) Evolution of the maximum emission intensity of Ce^{3+} (462 nm) and Mn^{2+} (680 nm) as a function of mol% (Mn) for $Ca_{0.997-y}Ce_{0.003}Mn_yCN_2$ co-doped samples ($0.003 \leq y \leq 0.04$). Uncertainty bar = ± 0.05.
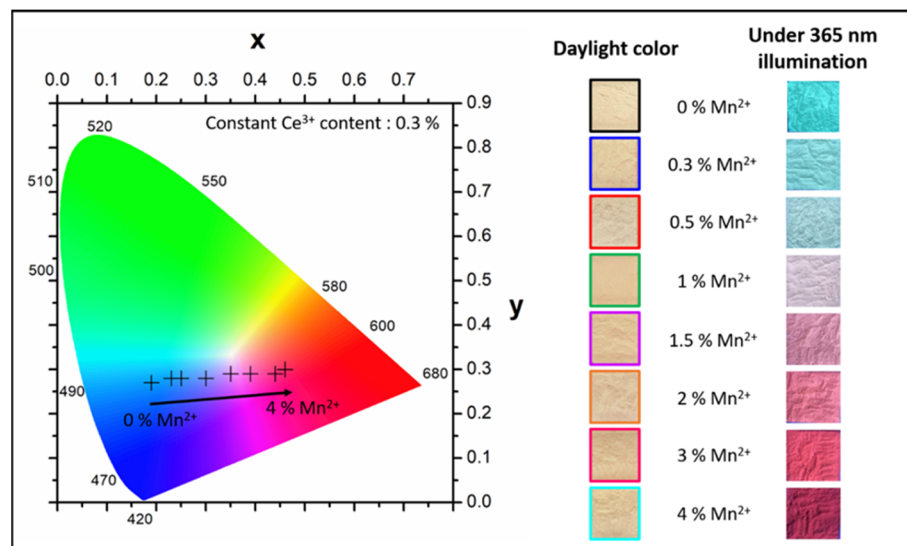

Figure 12. The CIE chromaticity diagram, chromaticity coordinates, and picture under 365 nm UV lamp at room temperature of $Ca_{0.997-y}Ce_{0.003}Mn_yCN_2$ ($0.003 \leq y \leq 0.04$) samples.

In order to further investigate the efficiency (η_T) of the energy transfers (ET) from Ce^{3+} to Mn^{2+}, the lifetime and the ET efficiency are calculated from the decay curves of $Ca_{0.997-y}Ce_{0.003}Mn_yCN_2$ ($0.003 \leq y \leq 0.04$)-doped samples monitored at 394 nm (Figure 13). The decay curves can be well fitted by a bi-exponential function, owing to the splitting of the 4f ground state of Ce^{3+}, $^2F_{5/2}$ and $^2F_{7/2}$ levels [34,35],

$$I = A_1 \exp\left(-\frac{t}{\tau_1}\right) + A_2 \exp\left(-\frac{t}{\tau_2}\right), \qquad (1)$$

where I is the luminescence intensity, A_1 and A_2 are constants, t is the time, and τ_1 and τ_2 are the decay constant for the exponential component. The average decay time is calculated with the following formula [34,35],

$$\tau = \left(A_1\tau_1{}^2 + A_2\tau_2{}^2\right)/\left(A_1\tau_1 + A_2\tau_2\right), \tag{2}$$
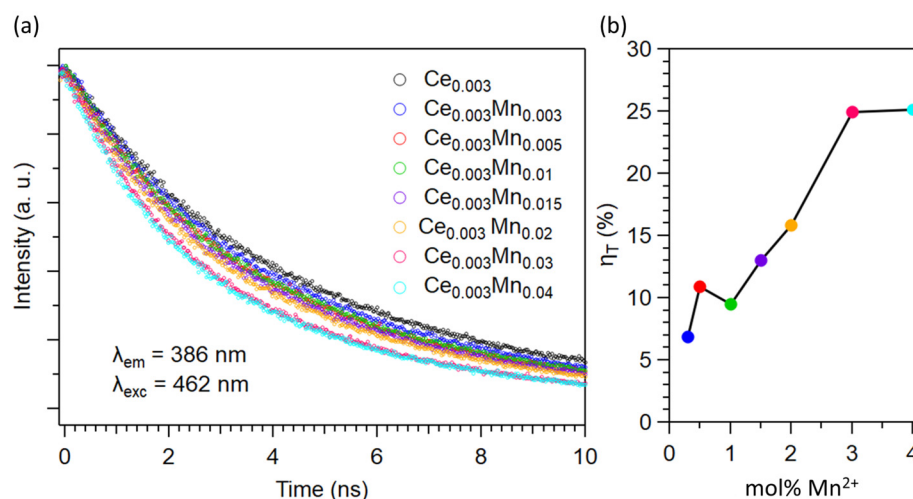
Figure 13. (**a**) Photoluminescence decay curves of Ce^{3+} in $Ca_{0.997-y}Ce_{0.003}Mn_yCN_2$ ($0.003 \leq y \leq 0.04$) samples. (**b**) Energy transfers efficiency (η_T) vs. mol% (Mn) for $Ca_{0.997-y}Ce_{0.003}Mn_yCN_2$ ($0.003 \leq y \leq 0.04$).

The decay time values τ are calculated to be 5.69 ns ($y = 0$), 5.30 ns ($y = 0.003$), 5.07 ns ($y = 0.005$), 5.15 ns ($y = 0.01$), 4.95 ns ($y = 0.015$), 4.79 ns ($y = 0.02$), 4.27 ns ($y = 0.03$) and 4.26 ns (y = 0.04), with an increase in Mn^{2+} content from 0% to 4%. It is clearly observed that the decay time tends to gradually decrease with increasing concentration of co-doped Mn^{2+}, which strongly supports the energy transfers from Ce^{3+} to Mn^{2+}. In addition, the ET efficiency from Ce^{3+} to Mn^{2+} was also investigated. Generally, the ET efficiency from sensitizer to activator can be calculated by using the following formula [36],

$$\eta_T = 1 - \frac{\tau_S}{\tau_{S0}}, \tag{3}$$

where τ_{S0} and τ_S are the decay lifetimes of the sensitizer (Ce^{3+}) in the absence and presence of the activator (Mn^{2+}), respectively.

As shown in the inset of Figure 13, the efficiency is found to increase gradually with increasing Mn^{2+} content up to 3 mol% (Mn) and then remains more or less constant up to 4 mol% (Mn). However, the Mn^{2+} emission intensity gradually decreases from 2 to 4 mol% (Mn). This indicates that the quantity of energy that can transfer from Ce^{3+} to Mn^{2+} is gradually restricted for high Mn^{2+} concentration due to the fixed Ce^{3+} concentration and Mn^{2+} concentration quenching effect.

In general, non-radiative energy transfers from a sensitizer to an activator take place via exchange interaction or electric multipolar interaction [37,38]. If the energy transfers result from the exchange interaction, the critical distance between the sensitizer and activator should be shorter than 4 Å. The critical distance R_C for energy transfers from Ce^{3+} to Mn^{2+} ions can be calculated from the following relationship given by Blasse [39],

$$R_C = 2\left(\frac{3V}{4\pi x_c N}\right)^{1/3}, \tag{4}$$

where V is the volume of the unit cell, x_c is the critical concentration, and N represents the number of sites that the doped ions can occupy in the unit cell.

The x_c is defined as the total concentration of the Ce^{3+} and Mn^{2+} dopant ions, at which the emission intensity of Ce^{3+} in $Ca_{0.997-y}Ce_{0.003}Mn_yCN_2$ is half of that in $Ca_{0.997}Ce_{0.003}CN_2$ phosphor. For the $CaCN_2$ host lattice, N = 3, x_c = 0.013, V = 174.6 $Å^3$. Therefore, the critical distance R_C (Ce^{3+}-Mn^{2+}) was calculated to be 20.45 Å. This value is much longer than 4 Å, indicating that the energy transfers between the Ce^{3+} and Mn^{2+} ions mainly take place via electric multipolar interactions.

On the basis of Dexter's energy transfers formula of multipolar interaction and Reisfeld's approximation, the following relation can be obtained [37,40]:

$$\frac{I_{S0}}{I_S} \propto C^{\alpha/3}, \tag{5}$$

where I_{S0} and I_S represent the luminescence intensities of the sensitizer Ce^{3+} ions without and with the presence of the Mn^{2+} ions, respectively. C is the total concentration of the Ce^{3+} and Mn^{2+} ions. α = 6, 8, and 10 correspond to dipole–dipole, dipole–quadrupole, and quadrupole–quadrupole interactions, respectively. The relationship between I_{S0}/I_S and $C^{\alpha/3}$ when α = 6, 8, 10 is shown in Figure 14. A linear relation was observed only when α = 6, indicating that the mechanism of energy transfers from the Ce^{3+} to Mn^{2+} ions in $CaCN_2$ host lattice are mainly due to a dipole–dipole interaction.
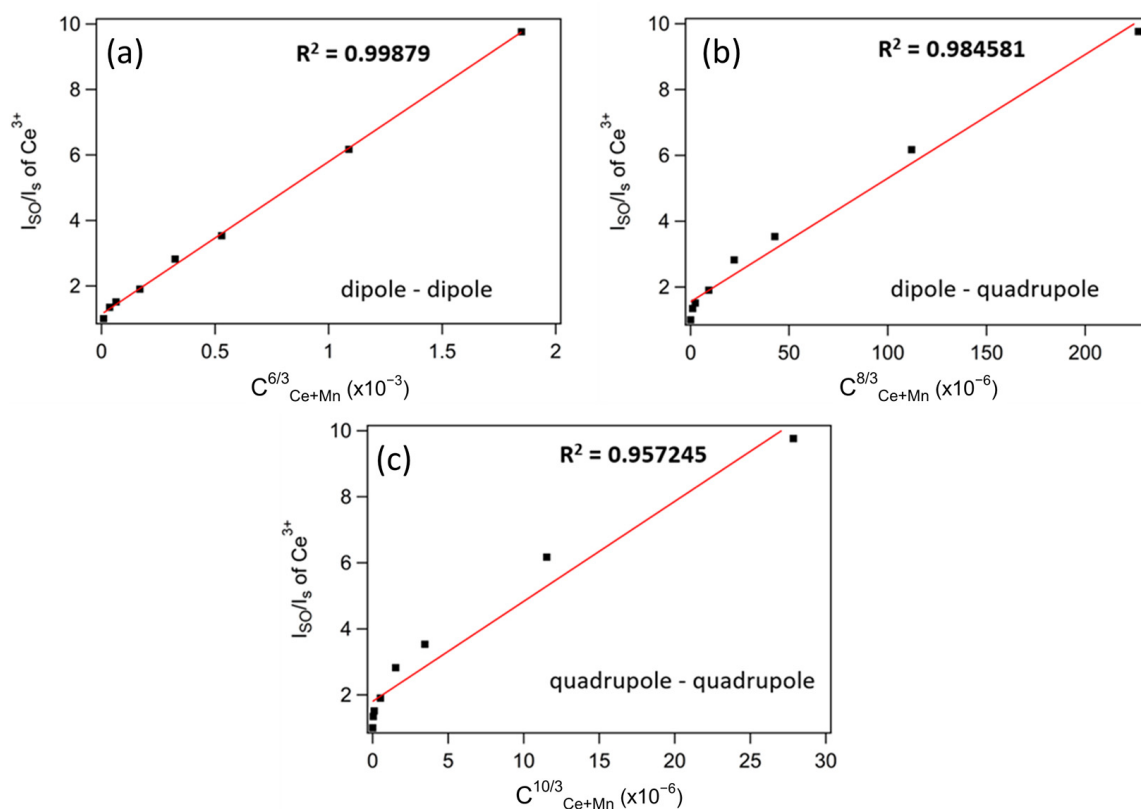
Figure 14. Dependence of I_{S0}/I_S of Ce^{3+} on (**a**) $C^{6/3}$, (**b**) $C^{8/3}$ and (**c**) $C^{10/3}$.

The thermal stability of phosphors is a key factor for their application in LEDs device. In general, under high-power operating conditions, the phosphors can reach temperatures up to 423 K [41]. Therefore, the effect of the temperature on the emission was investigated between 293 and 383 K under 386 nm excitation wavelength. As shown in Figure 15, the maximum emission intensity of $Ca_{0.987}Ce_{0.003}Mn_{0.01}CN_2$ decreases between 293 and 383 K by approximatively 80% and 67% for the Ce^{3+} (462 nm) and Mn^{2+} (680 nm) bands, respectively. This 80% diminution in intensity for the cerium band is comparable to that observed on the single-doped $Ca_{0.995}Ce_{0.005}CN_2$ sample. However, the decrease in intensity

of the manganese band is greater than that reported in our previous study for the single-doped $Ca_{0.96}Mn_{0.04}CN_2$ sample for which only a 20% decrease in the emission intensity at 680 nm was observed in the same conditions [20]. It should also be noted that the decreases in cerium and manganese emission intensities with increasing temperature are not proportional, leading to a variation in emission color with temperature. Additionally, the large decrease in the intensity of the manganese emission suggests the deactivation of the Ce^{3+} excited state before the energy transfers towards Mn^{2+} occur. The reduction in emission intensity at higher temperature is induced by higher probability of non-radiative processes such as thermal ionization through the conduction band of the host lattice and/or excitation energy migration among the dopants to quenching sites (e.g., vacancies and substitutional impurity atoms). It should also be noted that, as in the case of the single-doped $Ca_{0.995}Ce_{0.005}CN_2$ sample, the phenomenon is completely reversible.
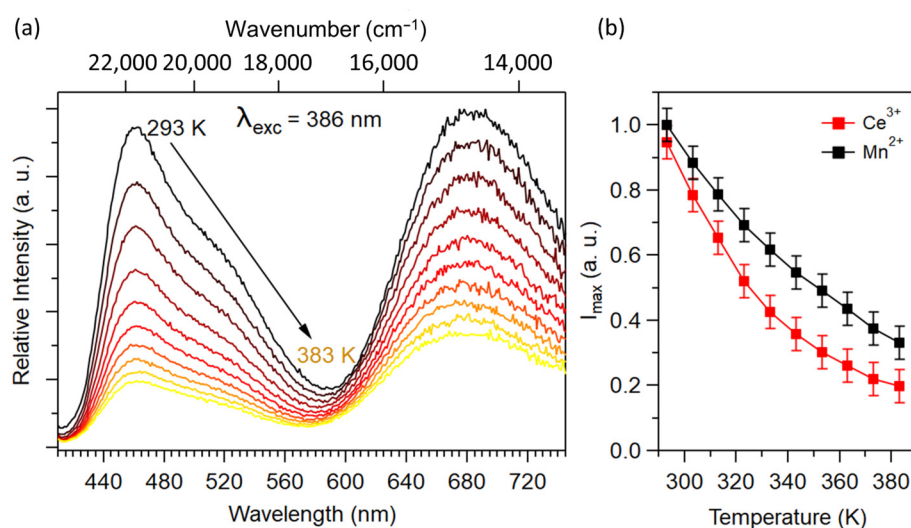
Figure 15. (**a**) PL spectra (λ_{exc} = 386 nm) of $Ca_{0.987}Ce_{0.003}Mn_{0.01}CN_2$ sample at variable temperature (293–383 K). (**b**) Maximum emission intensity (I_{max}) vs. temperature (293–387 K) for $Ca_{0.987}Ce_{0.003}Mn_{0.01}CN_2$. Uncertainty bars = ±0.05.

3. Materials and Methods

3.1. Preparation of Ce^{3+}, Mn^{2+} Co-Doped Calcium Carbodiimides

Powder samples of Ce^{3+}-doped $CaCN_2$ and Ce^{3+}/Mn^{2+} co-doped $CaCN_2$ were prepared by solid-state reactions from doped calcium carbonate and carbon nitride (C_3N_4) according to the synthesis route described in [16,20]. The nominal chemical compositions of the synthesized materials are $Ca_{1-x}Ce_xCN_2$ ($0 \leq x \leq 0.04$) and $Ca_{1-x-y}Ce_xMn_yCN_2$ (x = 0.003, $0.003 \leq y \leq 0.04$), respectively. Typically, doped calcium carbonates were prepared by co-precipitation method using $CaCl_2 \cdot 6H_2O$ (Aldrich, 98%), $Ce(NO_3)_3 \cdot 6H_2O$ (Alfa Aesar, 99.5%), $MnCl_2 \cdot 4H_2O$ (Alfa Aesar, 99%) and Na_2CO_3 (Acros Organics, 99.95%) as raw materials while carbon nitride was synthesized by heating melamine ($C_3H_6N_6$–Alfa Aesar, 99%) at 550 °C for 5 h in a closed alumina crucible in a muffle furnace. Then, the as-synthesized precursors were thoroughly mixed in an agate mortar and calcined at 700 °C for 1 h under ammonia flow (NH_3). Finally, the obtained powder was mixed again with C_3N_4 and annealed under similar conditions to guarantee the complete reaction between the carbonate and the carbon nitride. For more details on the synthesis of (co-doped) calcium carbonate, carbon nitride and (doped) carbodiimides, refer to our previous work [20].

3.2. Characterizations

X-ray powder diffraction (XRD) patterns were recorded at room temperature in the 10–90° 2θ range with a step size of 0.0261° and an effective scan time per step of 40 s using a PANalytical X'Pert Pro diffractometer (Cu-L2,L3 radiation, λ = 1.5418 Å, 40 kV, 40 mA,

PIXcel 1D detector). Data collector and HighScore Plus programs were used, respectively, for recording and analysis of the patterns. The XRD patterns for Rietveld refinements were collected at room temperature in the 5–120° 2θ range with a step size of 0.0131° and an effective scan time per step of 200 s. All calculations were carried out with Fullprof and WinPLOTR programs [42,43].

Nitrogen and oxygen contents were determined with a LECO TC-600 Analyzer using the inert gas fusion method in which nitrogen and oxygen contents were measured as N_2 by thermal conductivity and as CO_2 by infrared detection, respectively.

Powders morphology was examined by scanning electron microscopy (SEM) with a JEOL JSM 7100 F equipment operating at a 6 mm working distance, with an accelerating voltage of 20 kV. Energy dispersive X-ray spectroscopy (EDS) characterizations were performed using a JEOL IT300 microscope operating at a 10 mm working distance, with an accelerating voltage of 20 kV and a probe current of 7.45 nA. Sample preparation consisted in powder deposition on a carbon tape then metallization with gold.

Diffuse reflectance spectra were collected using a Varian Cary 100 Scan spectrometer equipped with a Varian WinUV software and a Labsphere DRA-CA-30I 70 mm integrating sphere. Experimental data were collected within the 200–800 nm range with a 1 nm step. Band gaps of the materials (E_g) were estimated using the Kubelka–Munk formalism [44].

Solid-state excitation and emission spectra were measured with a Horiba Jobin-Yvon Fluorolog-III fluorimeter equipped with a Xe lamp 450 W and a UV–Vis photomultiplier (Hamamatsu R928, sensitivity 190–860 nm). For the measurements recorded above room temperature, the samples were placed in an adequate solid holder then introduced in the F-3004 Jobin-Yvon heating Peltier module (293–383 K). Concerning the measurements recorded below room temperature (77–300 K), the luminescence has been measured on powder samples mounted directly onto copper plates using conductive silver glue and cooled with an optical cryostat (Oxford OptistatCF) coupled to a liquid nitrogen bath able to reach temperatures down to 77 K under nitrogen atmosphere. Luminescence decays were measured directly with the fluorescence spectrometer coupled with an additional TCSPC module (Time-Correlated-Single-Photon-Counting) and a 394 nm pulsed Delta-Diode. Quantum yields were measured using a G8 GMP integrating sphere according to $\Phi = (E_c - E_a)/(L_a - L_c)$, where E_c and L_c are the integrated emission spectrum and the absorption at the excitation wavelength of the sample and E_a and L_a are the integrated blank emission spectrum and blank absorption, respectively. Luminescence decays and quantum yields are the averages of three or five independent determinations. Appropriate filters were used to remove the laser light, the Rayleigh scattered light and associated harmonics from the emission spectra. All spectra were corrected for the instrumental response function. Colorimetric coordinates have been calculated on the basis of the emission spectra [45,46].

4. Conclusions

In summary, a series of Ce^{3+}-doped $CaCN_2$ and Ce^{3+}/Mn^{2+} co-doped $CaCN_2$ phosphors have been synthesized via a solid-state reaction using carbon nitride as a precursor. Investigations based on X-ray powder diffraction analysis attest the formation of high-purity and well-crystallized $Ca_{1-x}Ce_xCN_2$ ($0 \leq x \leq 0.04$) and $Ca_{0.997-y}Ce_{0.003}Mn_yCN_2$ ($0.003 \leq y \leq 0.04$) samples. Structural analysis also revealed a maximum solubility of Ce^{3+} approximately 2 mol% within the investigated dopant concentration, with the insertion of Ce^{3+} within the host structure by substitution for the Ca^{2+}. Under 386 nm excitation, Ce^{3+}-doped phosphors exhibit a broad blue emission band centered around 462 nm, with a shoulder at 510 nm, at room temperature. The optimized Ce^{3+} concentration of $CaCN_2:Ce^{3+}$ is 0.5 mol%. With increasing temperature, the emission intensity of the $Ca_{0.995}Ce_{0.005}CN_2$ sample decreases drastically on the order of 80% up to 387 K in a completely reversible manner. We also investigated the luminescence properties of $CaCN_2$ co-doped with Ce^{3+} and Mn^{2+}. The spectral characteristics and decay times indicate that efficient energy transfers occur between Ce^{3+} and Mn^{2+} via a non-radiative dipole–dipole mechanism. The critical

energy transfer distance has also been calculated by the concentration quenching method. Under near-ultraviolet excitation, the emission color of the obtained phosphors can be modulated from blue to red through a shade of white by adjusting the doping content of the Mn^{2+} ions with a fixed Ce^{3+} content, but the poor thermal stability of both the Ce^{3+} and Mn^{2+} emissions in the co-doped samples compared to the single-doped $CaCN_2:Mn^{2+}$ hinders their application in emitting devices.

Supplementary Materials: The following supporting information can be downloaded at: https://www.mdpi.com/article/10.3390/inorganics11070291/s1, Figure S1: Crystal structure of $CaCN_2$; Figure S2. Final Rietveld refinement pattern for $Ca_{0.995}Ce_{0.005}CN_2$; Figure S3: Deconvolution of the double emission band of $Ca_{0.995}Ce_{0.005}CN_2$; Figure S4: Powder X-ray diffraction diagrams of $Ca_{0.997-y}Ce_{0.003}Mn_yCN_2$ ($0.003 \leq y \leq 0.04$) samples; Figure S5. Final Rietveld refinement pattern for $Ca_{0.995}Ce_{0.003}Mn_{0.010}CN_2$; Figure S6: Evolution of the unit cell parameters (*a*, *c*) and cell volume (*V*) in $Ca_{0.997-y}Ce_{0.003}Mn_yCN_2$ ($0.003 \leq y \leq 0.04$) samples versus Ce^{3+} doping concentration; Table S1: Details of the Rietveld refinement of the XRD diagrams of the $Ca_{1-x}Ce_xCN_2$ samples; Table S2: Occupied Wyckoff sites, refined atomic coordinates (in Å), isotropic atomic displacement parameters B_{iso} (in Å^2) and site occupancies of $Ca_{1-x}Ce_xCN_2$ samples; Table S3: Details of the Rietveld refinement of the XRD diagrams of the $Ca_{0.997-y}Ce_{0.003}Mn_yCN_2$ ($0.003 \leq y \leq 0.04$) samples; Table S4: Chemical composition and Ce^{3+}, Mn^{2+} contents of $Ca_{0.997-y}Ce_{0.003}Mn_yCN_2$ ($0.003 \leq y \leq 0.04$) samples obtained using EDS and the inert gas fusion technique; Table S5: Chromaticity coordinates (*x*, *y*) of the $Ca_{0.997-y}Ce_{0.003}Mn_yCN_2$ ($0.003 \leq y \leq 0.04$) samples.

References

1. Li, K.; Shang, M.; Lian, H.; Lin, J. Recent Development in Phosphors with Different Emitting Colors via Energy Transfer. *J. Mater. Chem. C* **2016**, *4*, 5507–5530. [CrossRef]
2. Liang, C.; You, H.; Fu, Y.; Teng, X.; Liu, K.; He, J. A Novel Tunable Blue-Green-Emitting $CaGdGaAl_2O_7:Ce^{3+},Tb^{3+}$ Phosphor via Energy Transfer for UV-Excited White LEDs. *Dalton Trans.* **2015**, *44*, 8100–8106. [CrossRef]
3. Zielinska-Dabkowska, K.M. Make Lighting Healthier. *Nature* **2018**, *553*, 274–276. [CrossRef] [PubMed]
4. Downie, L.E.; Keller, P.R.; Busija, L.; Lawrenson, J.G.; Hull, C.C. Blue-light Filtering Spectacle Lenses for Visual Performance, Sleep, and Macular Health in Adults. *Cochrane Database Syst. Rev.* **2019**, *1*, 1–17. [CrossRef]
5. Ci, Z.; Sun, Q.; Sun, M.; Jiang, X.; Qin, S.; Wang, Y. Structure, Photoluminescence and Thermal Properties of Ce^{3+}, Mn^{2+} Co-Doped Phosphosilicate $Sr_7La_3[(PO_4)_{2.5}(SiO_4)_3(BO_4)_{0.5}](BO_2)$ Emission-Tunable Phosphor. *J. Mater. Chem. C* **2014**, *2*, 5850–5856. [CrossRef]
6. Wang, Z.; Li, P.; Guo, Q.; Yang, Z. A Single-Phased Warm White-Light-Emitting Phosphor $BaMg_2(PO_4)_2:Eu^{2+},Mn^{2+},Tb^{3+}$ for White Light Emitting Diodes. *Mater. Res. Bull.* **2014**, *52*, 30–36. [CrossRef]
7. Liu, W.-R.; Huang, C.-H.; Yeh, C.-W.; Tsai, J.-C.; Chiu, Y.-C.; Yeh, Y.-T.; Liu, R.-S. A Study on the Luminescence and Energy Transfer of Single-Phase and Color-Tunable $KCaY(PO_4)_2:Eu^{2+},Mn^{2+}$ Phosphor for Application in White-Light LEDs. *Inorg. Chem.* **2012**, *51*, 9636–9641. [CrossRef]
8. Zhang, J.; He, Y.; Qiu, Z.; Zhang, W.; Zhou, W.; Yu, L.; Lian, S. Site-Sensitive Energy Transfer Modes in $Ca_3Al_2O_6:Ce^{3+}/Tb^{3+}/Mn^{2+}$ Phosphors. *Dalton Trans.* **2014**, *43*, 18134–18145. [CrossRef]
9. Shang, M.; Li, C.; Lin, J. How to Produce White Light in a Single-Phase Host? *Chem. Soc. Rev.* **2014**, *5*, 1372–1386. [CrossRef]
10. Khan, S.A.; Khan, N.Z.; Sohail, M.; Ahmed, J.; Alhokbany, N.; Alshehri, S.M.; Xu, X.; Zhu, J.; Agathopoulos, S. Modern Aspects of Strategies for Developing Single-Phase Broadly Tunable White Light-Emitting Phosphors. *J. Mater. Chem. C* **2021**, *9*, 13041–13071. [CrossRef]

11. Glaser, J.; Unverfehrt, L.; Bettentrup, H.; Heymann, G.; Huppertz, H.; Jüstel, T.; Meyer, H.-J. Crystal Structures, Phase-Transition, and Photoluminescence of Rare Earth Carbodiimides. *Inorg. Chem.* **2008**, *47*, 10455–10460. [CrossRef]

12. Dutczak, D.; Ströbele, M.; Enseling, D.; Jüstel, T.; Meyer, H.-J. $Eu_2(CN_2)_3$ and $KEu[Si(CN_2)_4]$: Missing Members of the Rare Earth Metal Carbodiimide and Tetracyanamidosilicate Series. *Eur. J. Inorg. Chem.* **2016**, *2016*, 4011–4016. [CrossRef]

13. Dolabdjian, K.; Schedel, C.; Enseling, D.; Jüstel, T.; Meyer, H.-J. Synthesis, Luminescence and Nonlinear Optical Properties of Homoleptic Tetracyanamidogermanates $ARE[Ge(CN_2)_4]$ (A = K, Cs, and RE = La, Ce, Pr, Nd, Sm, Eu, Gd). *Z. Anorg. Allg. Chem.* **2017**, *643*, 488–494. [CrossRef]

14. Yuan, S.; Yang, Y.; Chevire, F.; Tessier, F.; Zhang, X.; Chen, G. Photoluminescence of Eu^{2+}-Doped Strontium Cyanamide: A Novel Host Lattice for Eu^{2+}. *J. Am. Ceram. Soc.* **2010**, *93*, 3052–3055. [CrossRef]

15. Krings, M.; Montana, G.; Dronskowski, R.; Wickleder, C. α-$SrNCN:Eu^{2+}$ − A Novel Efficient Orange-Emitting Phosphor. *Chem. Mater.* **2011**, *23*, 1694–1699. [CrossRef]

16. Leysour de Rohello, E.; Suffren, Y.; Merdrignac-Conanec, O.; Guillou, O.; Cheviré, F. Effect of Cationic Substitutions on the Photoluminescence Properties of Eu^{2+} Doped $SrCN_2$ Prepared by a Facile C_3N_4 Based Synthetic Approach. *J. Eur. Ceram. Soc.* **2020**, *40*, 6316–6321. [CrossRef]

17. Masubuchi, Y.; Nishitani, S.; Hosono, A.; Kitagawa, Y.; Ueda, J.; Tanabe, S.; Yamane, H.; Higuchi, M.; Kikkawa, S. Red-Emission over a Wide Range of Wavelengths at Various Temperatures from Tetragonal $BaCN_2:Eu^{2+}$. *J. Mater. Chem. C* **2018**, *6*, 6370–6377. [CrossRef]

18. Kubus, M.; Castro, C.; Enseling, D.; Jüstel, T. Room Temperature Red Emitting Carbodiimide Compound $Ca(CN_2):Mn^{2+}$. *Opt. Mater.* **2016**, *59*, 126–129. [CrossRef]

19. Leysour de Rohello, E.; Bour, F.; Suffren, Y.; Merdrignac-Conanec, O.; Guillou, O.; Cheviré, F. Synthesis and Photoluminescence Properties of Mn^{2+} Doped $ZnCN_2$ Phosphors. *Open Ceram.* **2021**, *7*, 100157. [CrossRef]

20. Leysour de Rohello, E.; Suffren, Y.; Merdrignac-Conanec, O.; Guillou, O.; Calers, C.; Cheviré, F. Synthesis and Photoluminescence Properties of Mn^{2+} Doped $Ca_{1-x}Sr_xCN_2$ Phosphors Prepared by a Carbon Nitride Based Route. *J. Solid State Chem.* **2021**, *300*, 122240. [CrossRef]

21. Schädler, H.D.; Jäger, L.; Senf, I. Pseudoelement Compounds. V. Pseudochalcogens—An Attempt of an Empirical and Theoretical Characterization. *Z. Anorg. Allg. Chem.* **1993**, *619*, 1115–1120. [CrossRef]

22. Pauling, L. *The Chemical Bond*; Cornell University Press: Ithaca, NY, USA, 1967.

23. Güthner, T.; Mertschenk, B. Cyanamides. In *Ullmann's Encyclopedia of Industrial Chemistry*; Wiley-VCH Verlag: Weinheim, Germany, 2006. [CrossRef]

24. Shannon, R.D. Revised Effective Ionic Radii and Systematic Studies of Interatomic Distances in Halides and Chalcogenides. *Acta Crystallogr. A* **1976**, *32*, 751–767. [CrossRef]

25. Vannerberg, N.G. The Crystal Structure of Calcium Cyanamide. *Acta Chem. Scand.* **1962**, *16*, 2263–2266. [CrossRef]

26. Zhu, Q.-Q.; Wang, L.; Hirosaki, N.; Hao, L.Y.; Xu, X.; Xie, R.-J. Extra-Broad Band Orange-Emitting Ce^{3+}-Doped $Y_3Si_5N_9O$ Phosphor for Solid-State Lighting: Electronic, Crystal Structures and Luminescence Properties. *Chem. Mater.* **2016**, *28*, 4829–4839. [CrossRef]

27. Ji, X.; Zhang, J.; Li, Y.; Liao, S.; Zhang, X.; Yang, Z.; Wang, Z.; Qiu, Z.; Zhou, W.; Yu, L.; et al. Improving Quantum Efficiency and Thermal Stability in Blue-Emitting $Ba_{2-x}Sr_xSiO_4:Ce^{3+}$ Phosphor via Solid Solution. *Chem. Mater.* **2018**, *30*, 5137–5147. [CrossRef]

28. Blasse, G.; Grabmaier, B.C. *Luminescent Materials*; Springer: Berlin/Heidelberg, Germany, 1994. [CrossRef]

29. Liu, Q.; Yin, H.; Liu, T.; Wang, C.; Liu, R.; Lü, W.; You, H. Luminescent Properties and Energy Transfer of $CaO:Ce^{3+},Mn^{2+}$ Phosphors for White LED. *J. Lumin.* **2016**, *177*, 349–353. [CrossRef]

30. Game, D.N.; Ingale, N.B.; Omanwar, S.K. Converted White Light Emitting Diodes from Ce^{3+} Doping of Alkali Earth Sulfide Phosphors. *Mater. Discov.* **2016**, *4*, 1–7. [CrossRef]

31. Yu, R.; Wang, J.; Zhang, M.; Zhang, J.; Yuan, H.; Su, Q. A New Blue-Emitting Phosphor of Ce^{3+}-Activated $CaLaGa_3S_6O$ for White-Light-Emitting Diodes. *Chem. Phys. Lett.* **2008**, *453*, 197–201. [CrossRef]

32. Bachmann, V.; Ronda, C.; Meijerink, A. Temperature Quenching of Yellow Ce^{3+} Luminescence in YAG:Ce. *Chem. Mater.* **2009**, *21*, 2077–2084. [CrossRef]

33. Wang, Z.; Lou, S.; Li, P. Enhanced Orange–Red Emission of $Sr_3La(PO_4)_3:Ce^{3+},Mn^{2+}$ via Energy Transfer. *J. Lumin.* **2014**, *156*, 87–90. [CrossRef]

34. Liu, H.; Liao, L.; Xia, Z. Structure, Luminescence Property and Energy Transfer Behavior of Color-Adjustable $La_5Si_2BO_{13}:Ce^{3+},Mn^{2+}$ Phosphors. *RSC Adv.* **2014**, *4*, 7288–7295. [CrossRef]

35. Si, J.; Wang, L.; Liu, L.; Yi, W.; Cai, G.; Takeda, T.; Funahashi, S.; Hirosaki, N.; Xie, R.-J. Structure, Luminescence and Energy Transfer in Ce^{3+} and Mn^{2+} Codoped γ-AlON Phosphors. *J. Mater. Chem. C* **2019**, *7*, 733–742. [CrossRef]

36. Paulose, P.I.; Jose, G.; Thomas, V.; Unnikrishnan, N.V.; Warrier, M.K.R. Sensitized Fluorescence of Ce^{3+}/Mn^{2+} System in Phosphate Glass. *J. Phys. Chem. Solids* **2003**, *64*, 841–846. [CrossRef]

37. Reisfeld, R.; Greenberg, E.; Velapoldi, R.; Barnett, B. Luminescence Quantum Efficiency of Gd and Tb in Borate Glasses and the Mechanism of Energy Transfer between Them. *J. Chem. Phys.* **2003**, *56*, 1698. [CrossRef]

38. Antipenko, B.M.; Batyaev, I.M.; Ermolaev, V.L.; Lyubimov, E.I.; Privalova, T.A. Radiationless Transfer of Electron Excitation Energy between Rare Earth Ions in $POCl_3$-$SnCl_4$. *Opt. Spektrosk.* **1970**, *29*, 335–338.

39. Blasse, G. Energy Transfer in Oxidic Phosphors. *Phys. Lett. A* **1968**, *28*, 444–445. [CrossRef]

40. Dexter, D.L. A Theory of Sensitized Luminescence in Solids. *J. Chem. Phys.* **1953**, *21*, 836–850. [CrossRef]
41. Lin, Y.-C.; Bettinelli, M.; Karlsson, M. Unraveling the Mechanisms of Thermal Quenching of Luminescence in Ce^{3+}-Doped Garnet Phosphors. *Chem. Mater.* **2019**, *31*, 3851–3862. [CrossRef]
42. Rodríguez-Carvajal, J. Recent Advances in Magnetic Structure Determination by Neutron Powder Diffraction. *Phys. B Condens. Matter* **1993**, *192*, 55–69. [CrossRef]
43. Roisnel, T.; Rodríguez-Carvajal, J. WinPLOTR: A Windows Tool for Powder Diffraction Pattern Analysis. *Mater. Sci. Forum* **2001**, *378*, 118–123. [CrossRef]
44. Kubelka, D.; Munk, L. Ein Beitrag Zur Optik Der Farbanstriche. *Z. Tech. Phys.* **1931**, *12*, 593–601.
45. Wyszecki, G. Colorimetry. In *Handbook of Optics*; Driscoll, W.G., Vaughan, W., Eds.; MacGraw-Hill Book Company: New York, NY, USA, 1978; pp. 1–15.
46. [CIE] International Commission on Illumination. *Method of Measuring and Specifying Colour Rendering Properties of Light Sources*; Publication No. CIE 13.3-1995; CIE: Vienna, Austria, 1995; 16p.